Research Article Vol. 34, No. 8 / August 2017 / Journal of the Optical Society of America B 1765

Journal of the Optical Society of America B

OPTICAL PHYSICS

On-chip high-sensitivity temperature sensor based on gain–loss coupled microresonators

Wenxiu Li,[1] Hao Zhang,[1,2] Jiaming Liu,[1] Jian Lin,[1] Xia Xue,[1] Xiaofu Zhang,[1] Xianfan Xu,[3] Anping Huang,[1] and Zhisong Xiao[1,*]

[1]Key Laboratory of Micro-Nano Measurement, Manipulation and Physics (Ministry of Education), School of Physics and Nuclear Energy Engineering, Beihang University, Beijing 100191, China
[2]School of Instrumentation Science and Opto-electronics Engineering, Beihang University, Beijing 100191, China
[3]Birck Nanotechnology Center, School of Mechanical Engineering, Purdue University, West Lafayette, Indiana 47907, USA
*Corresponding author: zsxiao@buaa.edu.cn

Received 16 March 2017; revised 18 June 2017; accepted 6 July 2017; posted 11 July 2017 (Doc. ID 290866); published 1 August 2017

Microcavities based on asymmetrical Fano resonance have great potential in the application of ultra-sensitive sensors. In this paper, a very sharp asymmetrical Fano resonance is achieved by indirectly coupled gain–loss cavities. The sensitivity for detecting temperature can be enhanced up to 10^7/K, 8 orders of magnitude greater than that for two indirectly coupled lossy cavities. The resolution of the thermal sensor reaches 10^{-13} K. A thermal sensing mechanism based on coupled gain–loss optical cavities is investigated theoretically. The integrated structure shows potential to be an ultra-sensitive temperature microsensor.

OCIS codes: (260.5740) Resonance; (230.4555) Coupled resonators; (130.6010) Sensors.

https://doi.org/10.1364/JOSAB.34.001765

1. INTRODUCTION

Optical microresonators with high Q factors and small mode volumes for sensing have received considerable attention in recent years for their potential applications in temperature [1–6], refractive index [7,8], pressure [9], biosensing [10–12], and rotation sensing [13–18]. Recent microresonator sensors have been based on the measurement of resonance frequency or resonance wavelength shifts due to the change of the environment parameters. For thermal sensor applications, the material properties of the resonator, such as thermal-optical effect and thermal expansion, are important for the resonance frequency shifts. Temperature sensors had previously been demonstrated on silica and silicon microresonators [1,6], but their sensitivity was limited by the small thermal-optical effect and thermal expansion. Therefore, high-Q-factor polydimethylsiloxane (PDMS)-coated microresonators with large thermal effect were used for the thermal sensors, resulting in sensitivity 1 order of magnitude higher than silica and silicon sensors [2,4].

Another sensing mechanism is through measuring the output intensity change with the resonance frequency or wavelength shifts. When measuring output intensity, Fano resonance is beneficial for improving sensitivity. In particular, Fano resonance with narrow and sharp asymmetrical line shapes has attracted attention for use in slow light [19,20], low switching threshold [21], and high-sensitivity sensors [7,8,22,23], which was first realized in side-coupled waveguide-cavity systems [24]. Since then, theoretical and experimental works have investigated asymmetric Fano resonance (AFR) in different configurations. In these experiments, AFR was generated in a single whispering-gallery microresonator (WGM) [25], and showed great potential for use in high-sensitivity sensors owing to its simple structure. Furthermore, dynamic Fano-like resonance in Er^{3+}-doped WGM microresonators for high-sensitivity sensors has been demonstrated by Yang *et al.* [26], providing experimental evidence of the Fano resonance in active cavities. In addition, Zhang [23] has realized high-temperature sensors using an eye-like ring resonator. A refractive index sensor with a two-lossy-cavity structure was proposed to produce sharp AFR [7], but the obtained slope of the asymmetric line shape was not sharp. Recently, the gain and loss engineering in cavities and waveguides have been investigated in nonlinearity [27,28], laser [29], and parity-time symmetry [30,31]. Fano resonace with large slope is obtained in a parity-time-assisted three-cavity configuration, and the slope is enhanced by 10^6 compared to that in Ref. [7].

In this paper, we propose an indirectly coupled gain–loss cavity configuration to generate AFR. The slope of the AFR is enhanced by 8 orders of magnitude in comparison with loss–loss coupled cavities, which is crucial to the sensitivity of temperature sensors. The paper is organized as follows. In Section 2, we theoretically analyze the reason for AFR formation in the proposed structure. In Section 3, we demonstrate the application of the gain–loss structure as an ultra-sensitive temperature sensor through numerical investigation.

2. THEORETICAL MODE AND ANALYSIS

The analyzed structure is shown in Fig. 1; it involves two resonant cavities with different effective decay rates. They are strongly coupled through an optical waveguide. As the distance L between cavity1 and cavity2 is much longer than the wavelength, no directly coupled mode exists among them. In the proposed configuration, the amplitude of the input and output field in the waveguide are represented by a_{in} and a_t, respectively. Due to the backscattering of the cavities, we define the reflection amplitude a_r, which can be detected in the input port.

To analyze the behavior of this configuration, we use the coupled mode theory [7,8,32,33]

$$\frac{dc_1}{dt} = -\left(i\omega_1 + \kappa_{E1} + \frac{\kappa_1}{2}\right)c_1 - g_{\text{eff}}c_2 - \sqrt{\kappa_{E1}}a_{\text{in}}, \quad (1)$$

$$\frac{dc_2}{dt} = -\left(i\omega_2 + \kappa_{E2} + \frac{\kappa_{I2}}{2}\right)c_2 - g_{\text{eff}}c_1 - e^{i\theta}\sqrt{\kappa_{E2}}a_{\text{in}}, \quad (2)$$

where the internal amplitudes in each cavity are represented by c_1 and c_2, ω_i $(i = 1, 2)$ is the resonance frequency of each cavity, and κ_{Ei} and κ_{Ii} are external and intrinsic decay rates, respectively. In cavity1, the effective intrinsic decay rate $\kappa_1 = \kappa_{I1} - g$ is reduced by the pump gain g [8], which can be provided by the rare-earth ions Er^{3+} or quantum dots [34,35]. For simplicity, we assume that the gain in cavity1 is $g = \xi\kappa_{I1}$. Therefore, the effective decay rate is $\kappa_1 = (1 - \xi)\kappa_{I1}$, which means that $\xi > 1$ and $\xi \le 1$ correspond to the gain and loss conditions, respectively, in cavity1. The effective interaction parameter $g_{\text{eff}} = e^{i\theta}\sqrt{\kappa_{E1}\kappa_{E2}}$ between the two cavities is dependent on the cavity–waveguide coupling rate κ_{Ei} $(i = 1, 2)$ and the propagating phase $\theta = kL$, where k is the propagation constant [7,8]. Experimentally, using the fiber taper to couple, the resonator can change the coupling coefficient κ_E by adjusting the gap between the fiber and the cavity. For control of the propagation phase θ, we can prepare a fabricated and free cavity, and the distance L between them can be adjusted arbitrarily by a translation stage [36]. Using the steady-state condition $dc_i/dt = -i\omega c_i$ in Eqs. (1) and (2), with the input light at the frequency ω, we can obtain the internal mode of each cavity:

$$c_1 = \frac{b_2\sqrt{\kappa_{E1}} + e^{2i\theta}\sqrt{\kappa_{E1}}\cdot\kappa_{E2}}{b_1 b_2 - e^{2i\theta}\kappa_{E1}\kappa_{E2}}a_{\text{in}}, \quad (3)$$

$$c_2 = \frac{e^{i\theta}\kappa_{E1}\sqrt{\kappa_{E2}} + e^{i\theta}b_1\sqrt{\kappa_{E2}}}{b_1 b_2 - e^{2i\theta}\kappa_{E1}\kappa_{E2}}a_{\text{in}}, \quad (4)$$

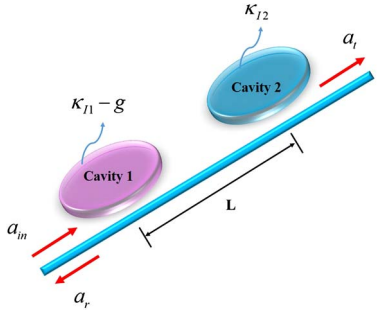

Fig. 1. Schematic of the coupled gain–loss cavities.

where $b_1 = i\Delta\omega_1 - \kappa_{E1} - \kappa_1/2$, $b_2 = i\Delta\omega_2 - \kappa_{E2} - \kappa_{I2}/2$, and $\Delta\omega_i = \omega - \omega_i$ is the frequency detuning. With the input and output relations [27]

$$a_r = \sqrt{\kappa_{E1}}c_1 + e^{i\theta}\sqrt{\kappa_{E2}}c_2, \quad (5)$$

$$a_t = \left(a_{\text{in}} + \sqrt{\kappa_{E1}}c_1\right)e^{i\theta} + \sqrt{\kappa_{E2}}c_2, \quad (6)$$

the transmission and reflection rates can be derived as

$$T_{\text{trans}} = \left|\frac{a_t}{a_{\text{in}}}\right|^2 = \left|\frac{e^{i\theta}(i\Delta\omega_1 - \kappa_1/2)(i\Delta\omega_2 - \kappa_{I2}/2)}{\left(i\Delta\omega_1 - \kappa_{E1} - \frac{\kappa_1}{2}\right)\left(i\Delta\omega_2 - \kappa_{E2} - \frac{\kappa_{I2}}{2}\right) - e^{2i\theta}\kappa_{E1}\kappa_{E2}}\right|^2, \quad (7)$$

$$R = \left|\frac{a_r}{a_{\text{in}}}\right|^2 = \left|\frac{e^{2i\theta}\left(i\Delta\omega_1 + \kappa_{E1} - \frac{\kappa_1}{2}\right)\kappa_{E2} + \left(i\Delta\omega_2 - \kappa_{E2} - \frac{\kappa_{I2}}{2}\right)\kappa_{E1}}{\left(i\Delta\omega_1 - \kappa_{E1} - \frac{\kappa_1}{2}\right)\left(i\Delta\omega_2 - \kappa_{E2} - \frac{\kappa_{I2}}{2}\right) - e^{2i\theta}\kappa_{E1}\kappa_{E2}}\right|^2. \quad (8)$$

As can be seen from Eq. (7), the added cavity2 introduces backward-propagating lights perturbing the phase of the transmission spectra and results in complex interference with the light transmission in the common waveguide [8,32], which is the reason for the AFR formation in this configuration. Assume that the parameters of the two cavities are identical, i.e., $\omega_1 = \omega_2$, $\kappa_{I1} = \kappa_{I2}$, and $\kappa_{E1} = \kappa_{E2} = 20\kappa_{I1}$ [8]. To demonstrate the characteristics of this coupled system, we display in Fig. 2 the transmission and reflection spectra of the two indirectly coupled cavities when the two cavities' resonance $\omega_1 = \omega_2$ and both spectra exhibit AFR with large slope. The gain–loss coupled cavities realize a sharper line shape than configuration with two lossy coupled cavities, that is, the interference of light radiated by both resonators with the pump light gives rise to a sharper AFR, which may have very steep frequency dependence. Physically, the gain in cavity1 compensates the loss of the coupled system and narrow-resonance line width, causing rapid changes in transmission and reflection spectra in very narrow frequency ranges. In practice, Er^{3+}-doped microresonators have become a mature technology to generate the gain, and there exists a minimum Er^{3+} concentration to

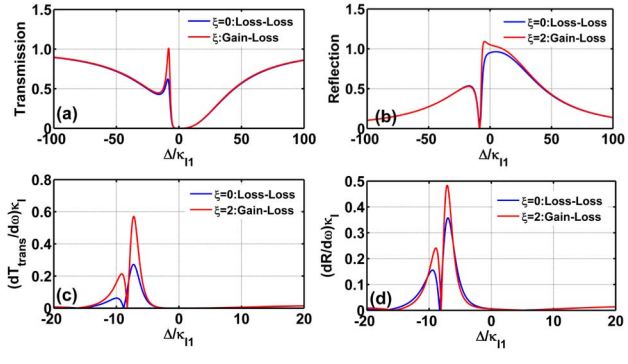

Fig. 2. (a) and (b) show transmission and reflection spectra, respectively, of the indirectly coupled cavities. Blue and red curves correspond to the loss–loss and gain–loss coupled conditions, respectively. (c) and (d) show slope of (a) and (b), respectively. Here, $\kappa_{I1} = \kappa_{I2}$, $\kappa_{E1} = \kappa_{E2} = 20\kappa_{I1}$, and $\theta = \pi/8$.

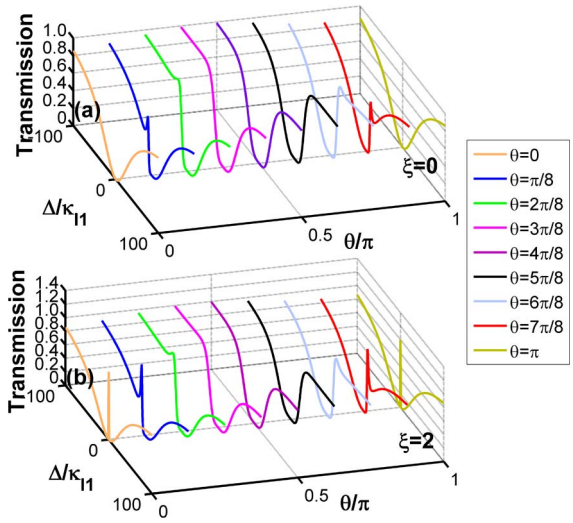

Fig. 3. Transmission spectra versus different propagation phase factors, where ($m = 0, 1, 2, 3, 4, 5, 6, 7, 8$). (a) and (b) are transmission spectra of loss–loss and gain–loss coupled cavities, respectively. Here, $\kappa_{I1} = \kappa_{I2}$, $\kappa_{E1} = \kappa_{E2} = 20\kappa_{I1}$.

produce enough gain to compensate the roundtrip loss for a fixed cavity Q factor. By changing the Er^{3+} concentration and the pump power, we can realize the gain variation. In [26,34,37], gain has been accurately controlled to compensate for the loss of the cavity.

Fano resonance is produced by the two resonances, involving interference via the optical waveguide, and the new resonant mode in each of the cavities and waveguide coupling strength are related to the propagating phase θ. This implies that asymmetric sharp transmission spectra can be produced by tuning the waveguide distance L between two cavities. Consequently, the transmission spectra of two lossy indirectly coupled cavities and gain–loss coupled cavities versus different θ are shown in the Fig. 3. The transmission spectra exhibit an asymmetric line shape for the properly propagated phase and realize a sharper line shape in gain–loss configuration with different propagation phase θ. Obviously, the transmission and reflection spectra at $\theta = m\pi$ (m is an integer) are symmetric Lorentz line shapes, in that the two resonance modes calculated by Eqs. (3) and (4) are degenerate. However, when $\theta = \pi/8 + m\pi$, an asymmetrical line shape is generated due to the distinct resonance interference. The reflection and transmission power at $\theta = \theta_a$ (θ_a is from 0 to π) and $\theta = \pi - \theta_a$ are horizontal mirror symmetric.

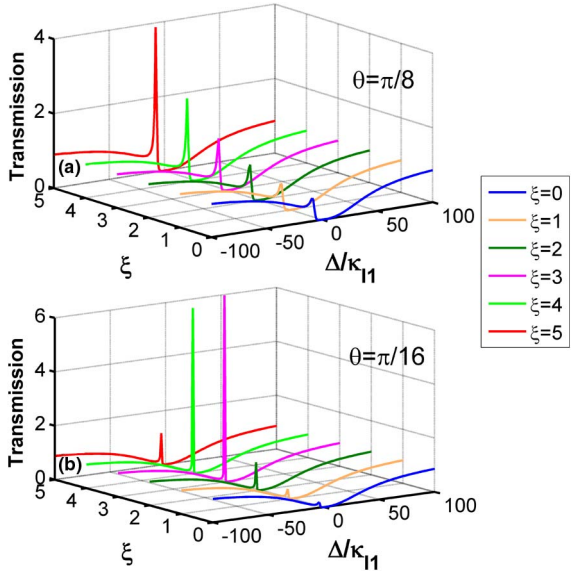

Fig. 4. Transmission spectra versus different gain parameters ξ. Here, $\kappa_{I1} = \kappa_{I2}$, $\kappa_{E1} = \kappa_{E2} = 20\kappa_{I1}$.

The transmission characteristics of the indirectly coupled structure at different ξ are depicted in Fig. 4. Specifically, different AFR spectra are obtained by modulating the ξ. In Fig. 4(a), a sharp resonance peak in the transmission spectra increases gradually with increase in ξ when $\theta = \pi/8$. However, the transmission increases until it reaches a maximum and then decreases gradually in Fig. 4(b). By optimizing the propagation phase θ and gain parameter ξ, we can obtain the maximum slope value of the AFR.

3. TEMPERATURE-SENSING MECHANISAM

Based on the preceding discussion, the sharper AFR causes the higher sensitivity. Here, the physical mechanism of the indirectly coupled cavity temperature sensors is discussed. When the coupled cavities come to a steady state, the thermal effect of the cavities resulting from the temperature changes relies on the refractive index n determined by the materials and diameter D of the cavities. The change of the resonance wavelength λ versus T in the WGM is [2,4]

$$\frac{d\lambda}{dT} = \lambda_0 \left[\frac{1}{n}\frac{dn}{dT} + \frac{1}{D}\frac{dD}{dT}\right], \tag{9}$$

where λ_0 is the resonance wavelength of the cold cavity and n is the effective refractive index; dn/dT is the thermo-optical coefficient and $(1/D)(dD/dT)$ is the thermal expansion coefficient. Hence, for a given input wavelength λ_0, the derivation of the normalized transmission signal can be expressed as

$$\frac{dT_{\text{trans}}}{dT} = -\frac{2\pi c}{\lambda_0}\left[\frac{1}{n}\frac{dn}{dT} + \frac{1}{D}\frac{dD}{dT}\right]\frac{dT_{\text{trans}}}{d\omega}, \tag{10}$$

where c is the light velocity in vacuum. dT_{trans}/dT defines the temperature-detection sensitivity of the coupled gain–loss cavities, and the slope is defined as

$$S = \left|\frac{dT_{\text{trans}}}{d\omega}\right|. \tag{11}$$

According to Eqs. (10) and (11), the detection sensitivity is directly proportional to transmission spectrum slope S, and larger S means greater temperature-detection sensitivity dT_{trans}/dT. Figure 5 shows the dependence of the maximum slope $S_{\max}$ by varying the values of θ with and without gain introduced in cavity1. The slope is sensitive to the propagation phase θ and the period of the slope is π, corresponding to the period of the transmission spectrum. All three curves in Fig. 5 have a minimum value at $\theta = m\pi$ (where m is an arbitrary integer), which is due to the transmission spectrum's symmetric Lorentzian line shape in this condition. The maximum $S_{\max}$ of each curve has been marked in Fig. 5 (see black arrows). As can

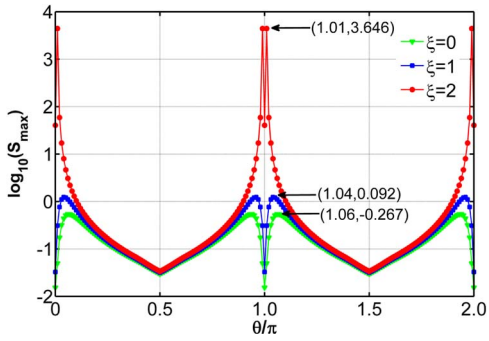

Fig. 5. Maximum slope S_{max} with various propagating phase factors θ/π. The green solid triangle, blue solid quadrate, and red solid dot correspond to the loss–loss ($\xi = 0$), critical ($\xi = 1$), and gain–loss balance ($\xi = 2$) conditions, respectively. $\kappa_{E1} = \kappa_{E2} = 20\kappa_{I1}$.

be seen, the gain–loss coupled structure (red curve) provides 3 orders of magnitude slope enhancement in comparison with the two lossy coupled cavities (green curve) at $\theta_c = \pm 0.01\pi + m\pi$. When θ approaches θ_c, the slope increases rapidly and reaches 10^3 in the gain–loss coupled condition.

The maximum value of slope S_{max} versus gain parameter ξ is depicted in Fig. 6. For a fixed propagating phase θ, when ξ increases, S_{max} increases slowly at first and then increases sharply, reaching the maximum value. All maximum values of sensitivity S_{max} are located at the region $\xi > 1$ (i.e., gain–loss coupled condition) and, with increasing propagating phase θ, the higher gain must be introduced to improve the slope of AFR. The slope gets a significant enhancement at $\xi = 2.35$, $\xi = 3.46$, and $\xi = 7.74$ when $\theta = \pi/32$, $\theta = \pi/16$, and $\theta = \pi/8$, respectively. It is essential to fix the gain at a specific value and, as a result, this will affect the functionality of the sensor dramatically, as shown in Fig. 7. As mentioned earlier, the gain variation is tuned by changing the Er^{3+} concentration and pump power. Furthermore, the method in Ref. [38] can accurately adjust and fix the gain coefficient, with an additional loss induced on the gain resonator, by a Cr-coated silica-nanofiber tip.

It is worth noting that the preceding analysis is based on the identical resonance frequency $\omega_1 = \omega_2$, at which resonators are coupled at same environment and neglect the nonlinear effect. However, the two cavities have a detuning $\omega_{12} = \omega_1 - \omega_2$ in practice. Both the slopes of the transmission spectra and the resonance peak intensity will decrease when two cavities have frequency difference ω_{12}, while the detection sensitivity will not degrade significantly when the two cavities have a frequency detuning ω_{12} shown in the inset of the Fig. 7(b). We also optimize the maximum slope of the AFR at detuning $\omega_{12} = 3\kappa_{I1}$ and find that the slope is 10^6. In addition, the cavity mode can be modulated by the electric-optical modulation or chemical etching [39], through which the detuning ω_{12} will be optimized to achieve the maximum slope.

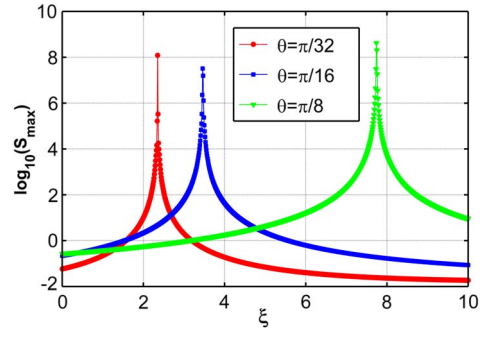

Fig. 6. Maximum slope S_{max} with various gain parameters ξ. $\xi \le 1$ and $\xi > 1$ correspond to the loss–loss and gain–loss coupled conditions, respectively. $\kappa_{I1} = \kappa_{I2}$, $\kappa_{E1} = \kappa_{E2} = 20\kappa_{I1}$.

Considering the actual parameters—input wavelength $\lambda = 1550$ nm, thermal-optical coefficient $dn/dT = 1.8 \times 10^{-4}$, thermal expansion coefficient $(1/D)(dD/dT) = -2.7 \times 10^{-4}$, effective refractive index $n = 1.37$, quality factor $Q = 10^6$, and intrinsic decay rate $\kappa_{I1} = 2\pi\omega/Q$—from Ref. [4], we can numerically calculate the detection sensitivity dT_{trans}/dT through the transmission spectra. The detection sensitivity dT_{trans}/dT in gain–loss coupled cavities can be numerically calculated as approaching 1.43×10^7/K from the highest value in Fig. 7, which means the transmitted spectrum will change 1.43 when the temperature changes 10^{-7} K. Thus, the gain introduction plays a key role in sensitivity of the temperature sensor based on microcavities.

In addition to sensitivity, minimum detectable signal with respect to noise is another important feature of the sensors. Either electrical or optical pumps will generate thermal noise and spontaneous emission noise (SPN) when we provide the gain in the resonator. Supposing the instrument can detect the power at the resolution of $(\Delta P)_{min}$, the minimum measured temperature is obtained as

$$(\Delta T)_{min} = \frac{(\Delta P)_{min}}{dP/dT} = \frac{(\Delta P)_{min}}{P_0 dT_{trans}/dT}, \tag{12}$$

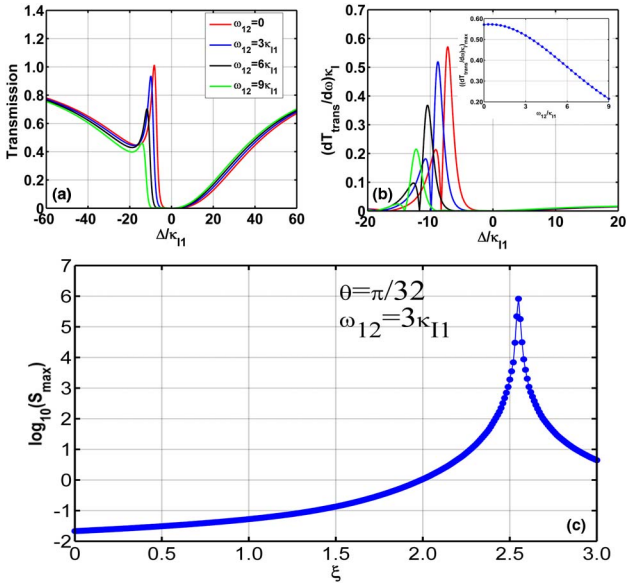

Fig. 7. (a) Transmission spectra in gain–loss coupled cavities when the two cavities have a detuning ω_{12}. (b) Slopes of (a); inset shows maximum slope as a function of ω_{12}. (c) Maximum slope S_{max} with various gain parameters ξ at detuning $\omega_{12} = 3\kappa_{I1}$.

Table 1. Formula of Noise Source [40]

Noise Source	Formula
Shot noise of detector	$I_{\text{shot}}^2 = 2B_e e(I_s + I_{\text{sp}})$
Thermal noise of detector	$I_{\text{th}}^2 = 4k_B T_{\text{eff}} B_e / R$
Spontaneous emission noise	$I_{\text{sp-sp}}^2 = (\eta I_{\text{sp}})^2 B_e (2B_0 - B_e)/B_0^2$
Signal-SPN beat noise	$I_{s\text{-sp}}^2 = 4I_s \eta^2 I_{\text{sp}} B_e / B_0$

Table 2. List of Simulation Parameters [25,40]

Parameter	Symbol	Value	Unit
Er^{3+} emission lifetime	τ_{21}	6	ms
Er^{3+} emission cross section	σ_{21}	6.33×10^{-25}	m^2
Plank constant	h	6.626×10^{-34}	J · S
Boltzmann constant	k_B	1.38×10^{-23}	J/K
Electric charge	e	1.6×10^{-19}	C
Temperature	T_{eff}	298.15	K
Quantum efficiency	η	0.6813	
Electrical bandwidth	B_e	10	Hz
Load resistance	R_L	500	Ω

where P_0 is the input power. The smallest detectable power changing is limited by the detector noises. The signal-to-noise ratio (SNR) of the thermal sensor can be expressed by $\text{SNR} = I_s/I_n$, in which $I_s = e\eta P_{\text{out}}/h\upsilon$ and $I_n = \sqrt{I_{\text{shot}}^2 + I_{\text{th}}^2 + I_{s\text{-sp}}^2 + I_{\text{sp}}^2}$ denote the detected signal and noise current [40], respectively, and all the terms of I_n shown in Table 1.

In the equations of Table 1, $I_{\text{sp}} = e\eta P_{\text{sp}}/h\upsilon$ is spontaneous emission noise current, P_{sp} is the spontaneous emission noise power (for details see Appendix A), B_0 denotes the optical bandwidth, B_e is the electrical bandwidth, η is the quantum efficiency, and R_L and T_{eff} are the resistance and temperature of the detector, respectively. All the values of the parameters are given in Table 2. When SNR = 1, the smallest detectable temperature under the noise limit is

$$(\Delta T)_{\min} = \frac{\sqrt{I_{\text{shot}}^2 + I_{\text{th}}^2 + I_{s\text{-sp}}^2 + I_{\text{sp}}^2}}{(e\eta/h\upsilon)P_0 dT_{\text{trans}}/dT}. \tag{13}$$

The total spontaneous emission noise current we calculate is $4.91 \times 10^{-18} A$ (for details see Appendix A), which is far less than the shot and thermal noise current. Therefore, we can neglect the influence of spontaneous emission noise on the temperature resolution. Figure 8 plots the influence of the noises on the detection limit. The thermal noise is dominant and the smallest detectable temperature change is mainly limited by it. The detection limit of the thermal sensor can be obtained as $(\Delta T)_{\min} = 10^{-13}$ K.

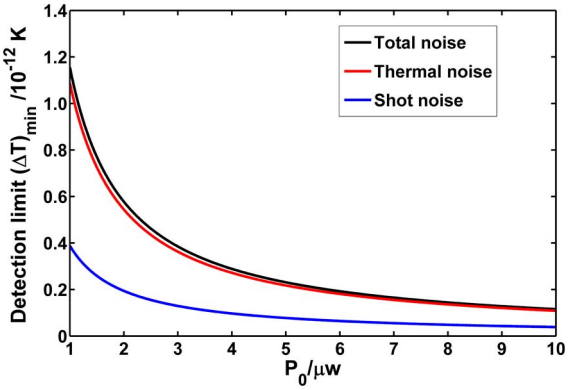

Fig. 8. Detection limit of the thermal sensor.

4. CONCLUSIONS

In summary, we theoretically investigated the evolution of the AFR in two configurations of gain–loss coupled cavities. Our results show that the gain–loss condition can greatly enhance the slope of the AFR, which gives larger transmission spectrum variation at a fixed resonance frequency than two lossy coupled cavities. This in turn shows such coupled microresonators to be promising thermal sensors with high sensitivity (10^7/K) and resolution (10^{-13} K). The investigated structure will enable ultra-high sensitivity and compact integrated microresonator sensors to become more feasible in practice.

APPENDIX A

To deal with the optical gain introduced in a resonator and the noise it generates, the typical coupled mode equation can be written as

$$\frac{da(t)}{dt} = \left(-i\Delta + \frac{1}{\tau_i} + \frac{1}{\tau_e}\right)a(t) - i\mu a_{\text{in}} - i\omega s(t), \tag{A1}$$

where $\Delta = \omega - \omega_0$, and $a(t)$ and $s(t)$ designate the amplitude of the resonant mode and the slowly varying amplitude of the noise, respectively. μ is the resonator–waveguide coupling strength and is equal to $\sqrt{1/\tau_e}$. The effective decay rate is $1/\tau_i = 1/\tau_g - 1/\tau_l$.

We assume the gain introduced in the resonator through Er^{3+} doping in the resonator. For simplicity, we consider the Er^{3+} two-level systems. N_1 and N_2 are the density of the erbium ions in the states $^4I_{13/2}$ and $^4I_{15/2}$, respectively, and N_1 is almost zero. Subsequently, a population inversion between the two states is formed to provide optical gain. The need to compensate the intrinsic loss τ_l in the cavity calls for the minimum population density for the upper level

$$N_2 = \frac{n_{\text{eff}}}{c\sigma_{21}\tau_c}, \tag{A2}$$

where σ_{21} is the emission cross-section of erbium ions and τ_c represents the cavity decay time calculated by $\tau_c = Ln_{\text{eff}}/[1 - \exp(-\alpha_{\text{int}}L)]c$, in which L represents the perimeter of the cavity and propagation loss is $\alpha_{\text{int}} = n_{\text{eff}}\omega/cQ_{\text{int}}$.

Then we can derive an equation for accumulating spontaneous emission based on the theory from Refs. [40,41]. Through Eqs. (A1) and (A2), the spontaneous emission power noise power of the resonator can be obtained as

$$P_{\text{sp}} = \frac{hR_{\text{sp}}}{\omega_0}\omega^2 \frac{1}{\left(\Delta^2 + \left(\frac{1}{\tau_i} + \frac{1}{\tau_e}\right)^2\right)^2} B_0, \tag{A3a}$$

$$R_{\text{sp}} = N_2 V_{\text{cav}}/\tau_{21}, \tag{A3b}$$

where B_0 is the optical bandwidth of the resonator, R_{sp} is the rate of spontaneous emission, V_{cav} is the cavity mode volume, and τ_{21} denotes the spontaneous emission time from the state $^4I_{13/2}$ to $^4I_{15/2}$.

Funding. International S and T Cooperation Program of China (2014DFA52000); National Natural Science Foundation of China (NSFC) (51372008, 11574021); Beijing Municipal Science and Technology Commission (Z161100000216149).

Acknowledgment. We thank Prof. Yunfeng Xiao for his useful comments and suggestions.

REFERENCES

1. M. Qiulin, T. Rossmann, and Z. Guo, "Whispering-gallery mode silica microsensors for cryogenic to room temperature measurement," Mater. Sci. Technol. **21**, 025310 (2010).
2. C. H. Dong, L. He, Y. F. Xiao, V. R. Gaddam, S. K. Ozdemir, Z.-F. Han, G.-C. Guo, and L. Yang, "Fabrication of high-Q polydimethylsiloxane optical microspheres for thermal sensing," Appl. Phys. Lett. **94**, 231119 (2009).
3. S. H. Nam and Y. Shizhuo, "High-temperature sensing using whispering gallery mode resonance in bent optical fibers," IEEE Photon. Technol. **17**, 2391–2393 (2005).
4. B.-B. Li, Q.-Y. Wang, Y.-F. Xiao, X.-F. Jiang, Y. Li, L. Xiao, and Q. Gong, "On chip high-sensitivity thermal sensor based on high-Q polydimethylsiloxane-coated microresonator," Appl. Phys. Lett. **96**, 251109 (2010).
5. D. V. Strekalov, R. J. Thompson, L. M. Baumgartel, and N. Yu, "Temperature measurement and stabilization in a birefringent whispering gallery mode resonator," Opt. Express **19**, 14495–14501 (2011).
6. Q. Ma, R. Tobias, and G. Zhixiong, "Temperature sensitivity of silica micro-resonators," J. Phys. D **41**, 245111 (2008).
7. Y.-F. Xiao, G. Venkat, and Y. Lan, "Coupled optical microcavities: an enhanced refractometric sensing configuration," Opt. Express **16**, 12538–12543 (2008).
8. J. Li, R. Yu, C. Ding, and Y. Wu, "PT-symmetry-induced evolution of sharp asymmetric line shapes and high-sensitivity refractive index sensors in a three-cavity array," Phys. Rev. A **93**, 023814 (2016).
9. S. Pevec and D. Donlagic, "Miniature all-fiber Fabry-Perot sensor for simultaneous measurement of pressure and temperature," Appl. Opt. **51**, 4536–4541 (2012).
10. K. De Vos, I. Bartolozzi, E. Schacht, P. Bienstman, and R. Baets, "Silicon-on-insulator microring resonator for sensitive and label-free biosensing," Opt. Express **15**, 7610–7615 (2007).
11. F. Vollmer and Y. Lan, "Review label-free detection with high-Q microcavities: a review of biosensing mechanisms for integrated devices," Nanophotonics **1**, 267–291 (2012).
12. G. C. Righini and S. Silvia, "Biosensing by WGM microspherical resonators," Sensors **16**, 905 (2016).
13. J. Scheuer and Y. Amnon, "Sagnac effect in coupled-resonator slow-light waveguide structures," Phys. Rev. Lett. **96**, 053901 (2006).
14. D. Hah and Z. Dan, "Analysis of resonant optical gyroscopes with two input/output waveguides," Opt. Express **18**, 18200–18205 (2010).
15. J. R. E. Toland, "Sagnac gyroscope using a two-dimensional array of coupled optical microresonators," Appl. Phys. B **114**, 333–339 (2014).
16. K. Z. Aghaie, V. Pierre-Baptiste, and J. F. D. Michel, "Rotation sensitivity analysis of a two-dimensional array of coupled resonators," Proc. SPIE **9378**, 93781P (2015).
17. H. Zhang, J. Liu, J. Lin, W. Li, X. Xue, A. Huang, and Z. Xiao, "On-chip tunable dispersion in a ring laser gyroscope for enhanced rotation sensing," Appl. Phys. A **122**, 1–6 (2016).
18. H. Zhang, J. Chen, J. Jin, J. Lin, L. Zhao, Z. Bi, A. Huang, and Z. Xiao, "On-chip modulation for rotating sensing of gyroscope based on ring resonator coupled with Mach-Zehnder interferometer," Sci. Rep. **6**, 19024 (2016).
19. M. F. Yanik, W. Suh, Z. Wang, and S. Fan, "Stopping light in a waveguide with an all-optical analog of electromagnetically induced transparency," Phys. Rev. Lett. **93**, 233903 (2004).
20. K. Totsuka, K. Norihiko, and T. Makoto, "Slow light in coupled-resonator-induced transparency," Phys. Rev. Lett. **98**, 213904 (2007).
21. L. Y. Mario, S. Darmawan, and M. K. Chin, "Asymmetric Fano resonance and bistability for high extinction ratio, large modulation depth, and low power switching," Opt. Express **14**, 12770–12781 (2006).
22. C.-Y. Chao and L. J. Guo, "Biochemical sensors based on polymer microrings with sharp asymmetrical resonance," Appl. Phys. Lett. **83**, 1527–1529 (2003).
23. Y. Zhang and X. Liu, "Eye-like ring resonator for highly sensitive temperature sensing," Proc. SPIE **8998**, 89980R (2014).
24. S. Fan, "Sharp asymmetric line shapes in side-coupled waveguide-cavity systems," Appl. Phys. Lett. **80**, 908–910 (2002).
25. B.-B. Li, Y.-F. Xiao, C.-L. Zou, Y.-C. Liu, X.-F. Jiang, Y.-L. Chen, Y. Li, and Q. Gong, "Experimental observation of Fano resonance in a single whispering-gallery microresonator," Appl. Phys. Lett. **98**, 021116 (2011).
26. F. Lei, B. Peng, S. K. Ozdemir, G. L. Long, and L. Yang, "Dynamic Fano-like resonances in erbium-doped whispering-gallery-mode microresonators," Appl. Phys. Lett. **105**, 101112 (2014).
27. M. H. Teimourpour, A. Rahman, K. Srinivasan, and R. El-Ganainy, "Non-Hermitian engineering of synthetic saturable absorbers for applications in photonics," Phys. Rev. A **7**, 014015 (2017).
28. B. He, S.-B. Yan, J. Wang, and M. Xiao, "Quantum noise effects with Kerr-nonlinearity enhancement in coupled gain-loss waveguides," Phys. Rev. A **91**, 053832 (2015).
29. M. H. Teimourpour, L. Ge, D. N. Christodoulides, and R. El-Ganainy, "Non-Hermitian engineering of single mode two dimensional laser arrays," Sci. Rep. **6**, 33253 (2016).
30. B. He, L. Yang, Z. Zhang, and M. Xiao, "Cyclic permutation-time symmetric structure with coupled gain-loss microcavities," Phys. Rev. A **91**, 033830 (2015).
31. M. H. Teimourpour, R. El-Ganainy, A. Eisfeld, A. Szameit, and D. N. Christodoulides, "Light transport in PT-invariant photonic structures with hidden symmetries," Phys. Rev. A **90**, 053817 (2014).
32. Y.-F. Xiao, M. Li, Y.-C. Liu, Y. Li, X. Sun, and Q. Gong, "Asymmetric Fano resonance analysis in indirectly coupled microresonators," Phys. Rev. A **82**, 065804 (2010).
33. B. E. Little, S. T. Chu, H. A. Haus, J. Foresi, and J.-P. Laine, "Microring resonator channel dropping filters," J. Lightwave Technol. **15**, 998–1005 (1997).
34. B. Peng, S. K. Özdemir, F. Lei, F. Monifi, M. Gianfreda, G. L. Long, S. Fan, F. Nori, C. M. Bender, and L. Yang, "Parity-time-symmetric whispering-gallery microcavities," Nat. Phys. **10**, 394–398 (2014).
35. K.-H. Kim, M.-S. Hwang, H.-R. Kim, J.-H. Choi, Y.-S. No, and H.-G. Park, "Direct observation of exceptional points in coupled photonic-crystal lasers with asymmetric optical gains," Nat. Commun. **7**, 13893 (2016).
36. B.-B. Li, Y.-F. Xiao, C.-L. Zou, X.-F. Jiang, Y.-C. Liu, F.-W. Sun, Y. Li, and Q. Gong, "Experimental controlling of Fano resonance in indirectly coupled whispering-gallery microresonators," Appl. Phys. Lett. **100**, 021108 (2012).
37. L. Chang, X. Jiang, S. Hua, C. Yang, J. Wen, L. Jiang, G. Li, G. Wang, and M. Xiao, "Parity-time symmetry and variable optical isolation in active-passive-coupled microresonators," Nat. Photonics **8**, 524–529 (2014).
38. B. Peng, Ş. K. Özdemir, S. Rotter, H. Yilmaz, M. Liertzer, F. Monifi, C. M. Bender, F. Nori, and L. Yang, "Loss-induced suppression and revival of lasing," Science **346**, 328–332 (2014).
39. C. E. Png, S. P. Chan, S. T. Lim, and G. T. Reed, "Optical phase modulators for MHz and GHz modulation in silicon-on-insulator (SOI)," J. Lightwave Technol. **22**, 1573–1582 (2004).
40. J. Chen, H. Zhang, J. Jin, J. Lin, L. Zhao, Z. Bi, A. Huang, and Z. Xiao, "Miniaturized optical gyroscope using active three-dimensional vertically coupled resonators," Opt. Eng. **54**, 107106 (2015).
41. J. K. S. Poon and A. Yariv, "Active coupled-resonator optical waveguides. I. Gain enhancement and noise," J. Opt. Soc. Am. B **24**, 2378–2388 (2007).